V International Scientific and Technical Conference Actual Issues of Power Supply Systems

Investigating the Enhanced Thermal Potential and Flow Characteristics of a Next-Generation Solar Dryer Design

AIPCP25-CF-ICAIPSS2025-00449 | Article

Investigating the Enhanced Thermal Potential and Flow Characteristics of a Next-Generation Solar Dryer Design

Dilmurod Mukhtorov [a)], Kambarali Ahunov, Abdullajon Khomidov, Nematulla Karimov, Musulmonkul Mamadaliev

Fergana State Technical University, 150100, Fergana, Uzbekistan

[a)] Corresponding author: dimajone0909@gmail.com

Abstract. This study focuses on analyzing the thermal and hydrodynamic characteristics of a new-generation solar dryer construction protected by Patent No. FAP 2604. To thoroughly understand the device's internal processes, a high-accuracy three-dimensional numerical modeling was performed using the COMSOL MULTIPHYSICS 6.1 software, and the results were successfully validated against experimental tests conducted with a thermal camera. The validation revealed that the relative error was between 2.5 % and 3.8 %, confirming the high reliability of the methodology used. Analyses indicated that this new construction is capable of accumulating high temperatures, up to 83.0ºC, on the absorber surface. Hydrodynamic analyses showed that the air velocity V profiles reach up to 0.6 m/s in several zones. This synergy of velocity and high temperature forms the basis for the device's efficient operation. In conclusion, the new construction has been scientifically substantiated as sufficiently reliable and possessing high thermal potential for practical implementation, offering a novel solution for the effective drying of agricultural products in the future..

INTRODUCTION

The utilization of solar energy is crucial for ensuring ecological sustainability and diversifying renewable energy sources. Solar collectors represent a key component within the spectrum of these technologies [1]. The utilization of collectors in solar dryers significantly enhances the thermal efficiency of the system, the drying kinetics, and the overall device performance [2]. Furthermore, reducing the use of fossil fuels and natural gas leads to a decrease in environmental pollution and a reduction in global greenhouse gas emissions [3]. The main components of existing solar dryer designs can be divided into several general categories based on the heating mode or the operational regime of heat derived from solar radiation and its subsequent use for removing moisture from the wet product [4]. In general manner, solar dryers are classified into active and passive dryers and each classification is divided into direct, indirect and mixed mode type [5,6,7]. The existing models are taking essentially two ways: the first approach studies particularly the behaviour of the product during the process represented by the drying kinetic. The second approach studies the general behaviour of the solar dryer by applying heat and mass transfers [8]. Numerous indirect solar dryers have been designed and constructed; however, their utilization is still limited due to their poor performance [9].

Considering the above, an analysis of the thermal processes was conducted within the physical model of solar dryers integrated with the proposed solar-air collector.

MATERIALS AND METHODS

In the proposed designs, the efficient discharge of vapor into the atmosphere is achieved via an ejector system utilizing natural convection. The pressure difference (gradient) created by the ejector and the device wall ensures the intensive removal of moisture separated from the product due to excessive heat. This solution does not require additional energy consumption for forced ventilation of the chamber, while simultaneously ensuring maximum vapor discharge efficiency.

The study investigated the newly developed construction of a solar dryer. Three-dimensional (3D) numerical modeling was performed using the 'COMSOL MULTIPHYSICS 6.1' software to analyze the thermal and hydrodynamic properties of the device.

RESULTS

Mathematical modeling of heat transfer processes in the proposed mixed-mode solar dryer based on a transparent polyethylene film.

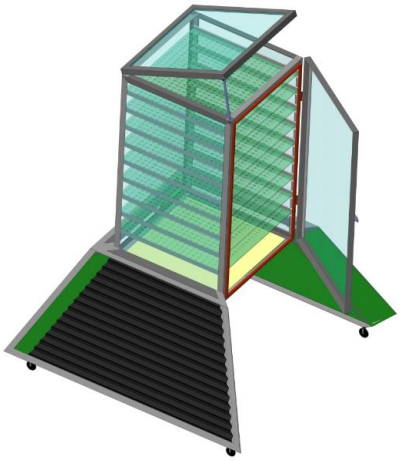

Fig.1. View of the proposed solar dryer

Mathematical modeling was employed to determine the optimal geometric parameters of the solar dryer shown in Figure 1 above. Several different models and approaches exist for the mathematical modeling of heat transfer processes in dryers equipped with solar air collectors.

As a result of the study, it can be particularly noted that the flow state, based on Reynolds experiments, can be determined using the following formula, which is characterized by the Reynolds number.

$$\mathrm{Re} = \frac{UL}{\nu}, \tag{1}$$

Where: L-is the characteristic length, U-is the characteristic velocity, and ν-is the kinematic viscosity coefficient [10].

The Reynolds number describes the relationship between inertial forces and viscous forces. If the inertial forces are smaller than the viscous forces, the flow represents a laminar flow regime.

If this ratio is large, meaning the inertial forces dominate the viscous forces, the flow becomes unstable and disturbances destroy the ordered structure characteristic of laminar flow, leading to a turbulent flow regime.

Turbulent flow can be represented as a collection of eddies (vortices) rotating in various directions and planes. Large eddies are transformed into smaller eddies, which in turn, specifically those whose size is slightly larger than the mean free path of a molecule, convert their energy into viscous heat energy.

Taking into account the relationship between laminar and turbulent air movements mentioned above, a mathematical model was developed for the longitudinal temperature distribution in the solar air collector, which directly depends on the air velocity.

The Navier-Stokes, energy conservation (temperature distribution), and mass conservation equations are presented below in tensor form [11].

Direct numerical simulation (DNS) of the Navier-Stokes equation requires the Reynolds number to be very small. Taking this into account, the time-averaged Navier-Stokes equation, as introduced by Reynolds, is utilized.

$$\begin{cases} \rho\dfrac{\partial\overline{u_i}}{\partial t}+\rho\dfrac{\partial\left(\overline{u_i}\,\overline{u_j}\right)}{\partial x_j}=-\dfrac{\partial\overline{p}}{\partial x_i}+\mu\dfrac{\partial^2\overline{u_i}}{\partial x_j\partial x_j}, \\ \dfrac{\partial\overline{T}}{\partial t}+\dfrac{\partial\left(\overline{u_i}\overline{T}\right)}{\partial x_j}=\kappa\dfrac{\partial^2\overline{T}}{\partial x_j\partial x_j} \\ \dfrac{\partial\overline{u_j}}{\partial x_j}=0, \quad (i,j=1,2,3). \end{cases} \tag{2}$$

The tensor form of the Reynolds equation and the energy distribution equation after applying the Boussinesq hypothesis is presented below: [12]:

Where $\overline{u_i}$ - is the flow velocity, $\overline{T}$ - is the temperature, ν, ν_t - is the laminar and turbulent viscosity, and $\kappa=\dfrac{1}{\mathrm{Pr}}$, $\kappa_t=\dfrac{1}{\mathrm{Pr}_t}$ - is the Prandtl number for laminar and turbulent flow.

$$\begin{cases} \dfrac{\partial\overline{u_i}}{\partial t}+\dfrac{\partial\left(\overline{u_i}\,\overline{u_j}\right)}{\partial x_j}=-\dfrac{\partial\overline{p}}{\rho\partial x_i}+\dfrac{\partial}{\partial x_j}\left(\left(\nu+\nu_t\right)\dfrac{\partial\overline{u_i}}{\partial x_j}\right), \\ \dfrac{\partial\overline{T}}{\partial t}+\overline{u_i}\dfrac{\partial\overline{T}}{\partial x_j}=\dfrac{\partial}{\partial x_j}\left(\left(\kappa+\kappa_t\right)\dfrac{\partial\overline{T}}{\partial x_j}\right) \\ \dfrac{\partial\overline{u_j}}{\partial x_j}=0, \quad (i,j=1,2,3). \end{cases} \tag{3}$$

Unknown terms, known as Reynolds stresses, arise in the Reynolds equation presented above. Currently, numerous semi-empirical models exist for determining these Reynolds stresses [13].

In physics, the Spalart–Allmaras model is a one-equation model that solves the modeled equation (2) for kinematic turbulent viscosity. The Spalart–Allmaras model was specifically designed for aerospace applications involving wall-bounded flows and has been shown to yield good results for boundary layers subjected to adverse pressure gradients. Furthermore, it also provides a very good estimation of the turbulent diffusion equation.

The highly-rated Spalart–Allmaras model was applied in this research work. The differential form of this model is as follows [14]:

The turbulent viscosity coefficient is determined as follows:

$$\frac{\partial\tilde{v}}{\partial t}+u_j\frac{\partial\tilde{v}}{\partial x_j}=C_{b1}(1-f_{t2})\tilde{S}\tilde{v}-\left[C_{w1}f_w-\frac{C_{b1}}{k^2}f_{t2}\right]\left(\frac{\tilde{v}}{d}\right)^2+$$
$$+\frac{1}{\sigma}\left[\frac{\partial}{\partial x_j}\left((v+\tilde{v})\frac{\partial\tilde{v}}{\partial x_j}\right)+C_{b2}\frac{\partial\tilde{v}}{\partial x_i}\frac{\partial\tilde{v}}{\partial x_i}\right]. \tag{4}$$

$$\nu_t=\tilde{v}f_{v1}. \tag{5}$$

Where: Ω - is the eddy viscosity, $\widetilde{S}$ - is the velocity deformation, and d- is the nearest distance to the wall.

$$f_{v1}=\frac{x^3}{x^3+c_{v1}^3},\overrightarrow{\leftarrow}\overrightarrow{\leftarrow}\overrightarrow{\leftarrow}\overrightarrow{\leftarrow}\overrightarrow{\leftarrow}\ x=\frac{\tilde{v}}{v},\tilde{S}=\Omega+\frac{\tilde{v}}{k^2d^2}f_{v2}. \tag{6}$$

The additional functions and constants of the model are as follows:

$$\Omega = \sqrt{2W_{ij}W_{ij}} \tag{7}$$

$$f_w = g\left[\frac{1+C_{w3}^6}{g^6+C_{w3}^6}\right], \quad g = r + C_{w2}(r^6 - r),$$

$$f_{v2} = 1 - \frac{x}{1+xf_{v1}}, g = r + c_{w2}(r^6 - r),$$

$$f_{t2} = c_{t3}\exp(-c_{t4}x^2), \qquad r = \min\left[\frac{\widetilde{\nu}}{\widetilde{S}k^2d^2}, 10\right], \tag{8}$$

$$W_{ij} = \frac{1}{2}\left(\frac{\partial U_i}{\partial x_j} - \frac{\partial U_j}{\partial x_i}\right).$$

Table 1. Model constant

σ_v	k_r	C_{b1}	C_{b2}	C_{v1}	C_{w1}	C_{w2}	C_{w3}	C_{r1}	C_{r2}	C_{r3}
2/3	0.41	0.1335	0.622	7.1	$C_{w1} = \frac{C_{b1}}{k^2} + \frac{1+C_{b2}}{\sigma}$	0.3	2.0	1	12	1

In solar air heater dryers, it is first required to construct the computational grids. The computational grid has the following appearance:

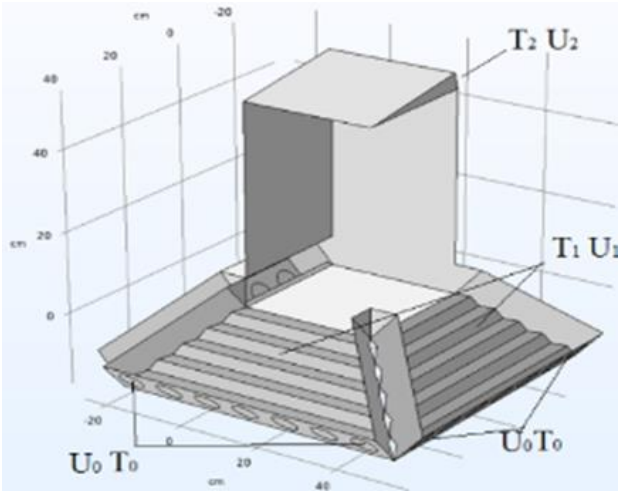

Fig. 2. Computational grid

In order to increase the accuracy of the calculation, the computational domain of the device was divided into a total of 2,760,235 nodes.

Where: T_o- is the inlet air temperature in *K*, T_1- s the temperature of the absorber surface, T_2- is the air temperature at the device outlet, U_o- is the air velocity at the inlet, U_1- is the air velocity at the wall, and T_2- is the air velocity at the outlet.

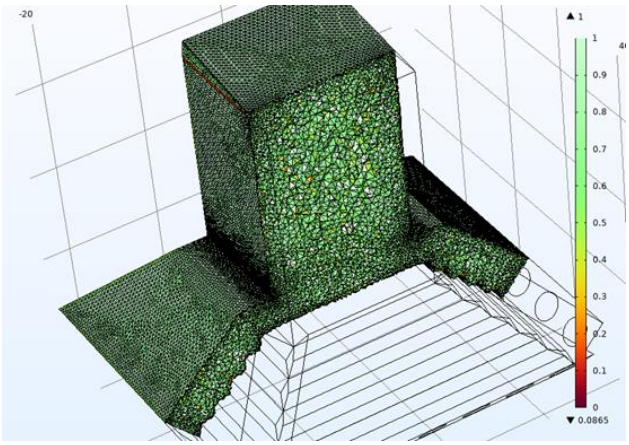

Fig.3. Boundary conditions

Boundary conditions

For air velocity, the no-slip condition at the walls is $\overline{u_i} = 0$. Q The extrapolation condition at the device outlet is $\frac{\partial^2 \overline{u_j}}{\partial x^2{}_j} = 0$. Here, the air velocity arises due to density changes, thus the inlet air velocity is derived from the governing equation. For temperature, the ambient air temperature is specified at the inlet as $T = T_0$. The extrapolation condition is applied to determine the air temperature at the outlet, $\frac{\partial^2 T}{\partial x^2{}_j} = 0$. The temperature of the absorber surface is determined from the solar radiation. Boundary conditions for pressure are derived from the RANS equation. For the Spalart–Allmaras model, the inlet value is equal to 3v.

In the air heater collectors of the dryer, the air flow washes over the working chamber's absorber surface, which increases the heat exchange efficiency. Considering the change in the heat transfer coefficient in accordance with the surface temperature and air mass flow rate, the time-dependent heat distribution in the collector is as follows:

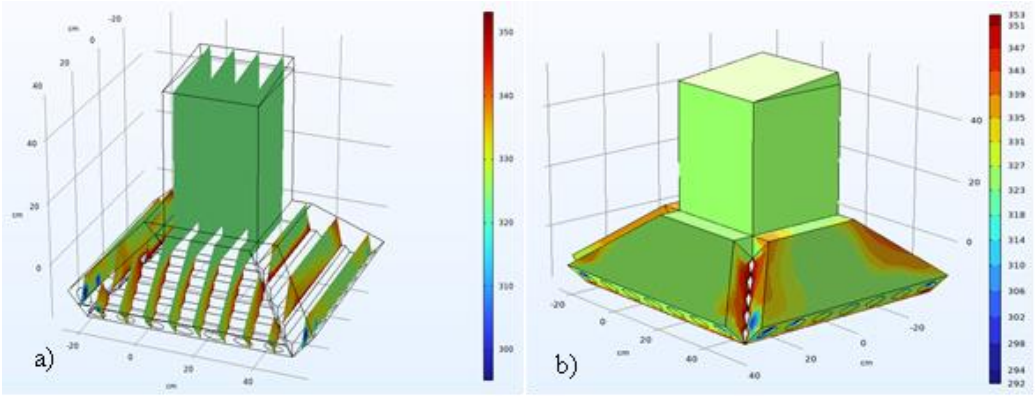

Fig. 4. Isoline of temperature distribution
a) Cross-sectional temperature slices, b) Surface temperature gradient.

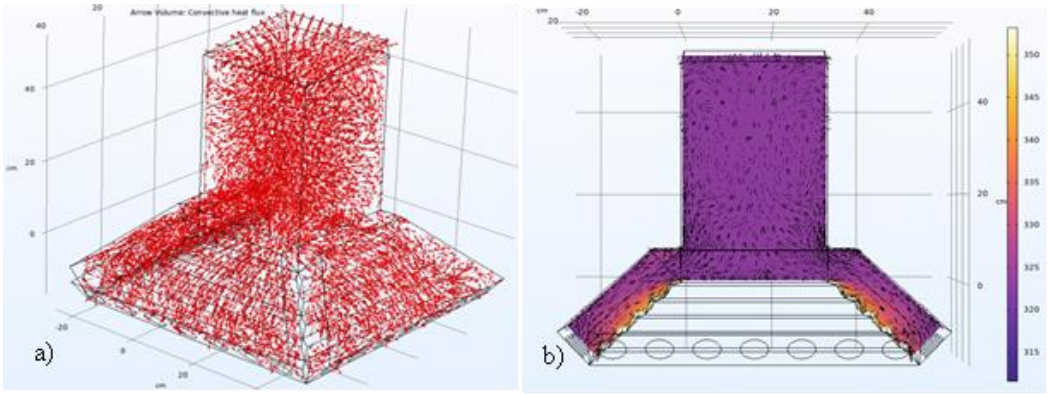

Fig. 5. Convective heat flow
a) Multislice temperature distribution, b) Volumetric temperature gradient.

As a result of constructing the isoline of the overall temperature distribution in the dryer's main working chamber, it became possible to determine the points of general heat distribution.

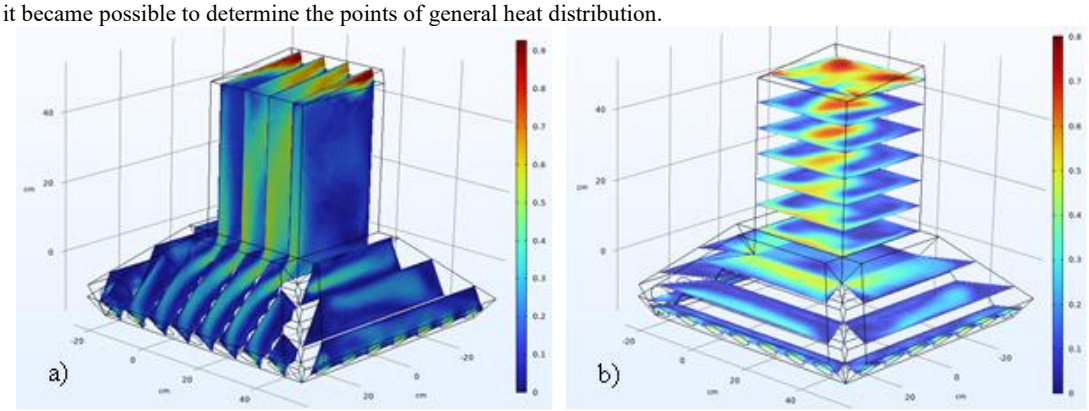

Fig. 6. Isoline of velocity
a) Velocity gradient along vertical slices, b) Velocity fields across horizontal planes.

In order to determine the optimal operating regimes of the device, the isoline of the overall velocity distribution in the device was constructed, which made it possible to ascertain the flow movement at general points. Based on the results obtained, the optimal air flow movement regimes within the device were determined.

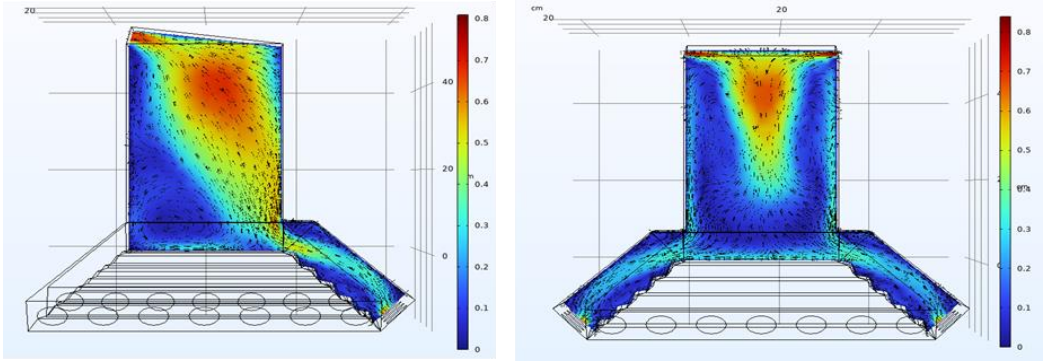

Fig. 7. Direction of velocity distribution
a) Flow trajectory in the side cross-section, b) Flow distribution in the front cross-section

Determining the thermal processes, including heat and velocity distribution processes, occurring in the dryer's working chamber allows for the identification of the device's optimal operating regime, as the drying process of all types of products directly depends on the heat distribution and the air flow velocity.

The results of the numerical experiments obtained from the developed mathematical model are presented in the next section.

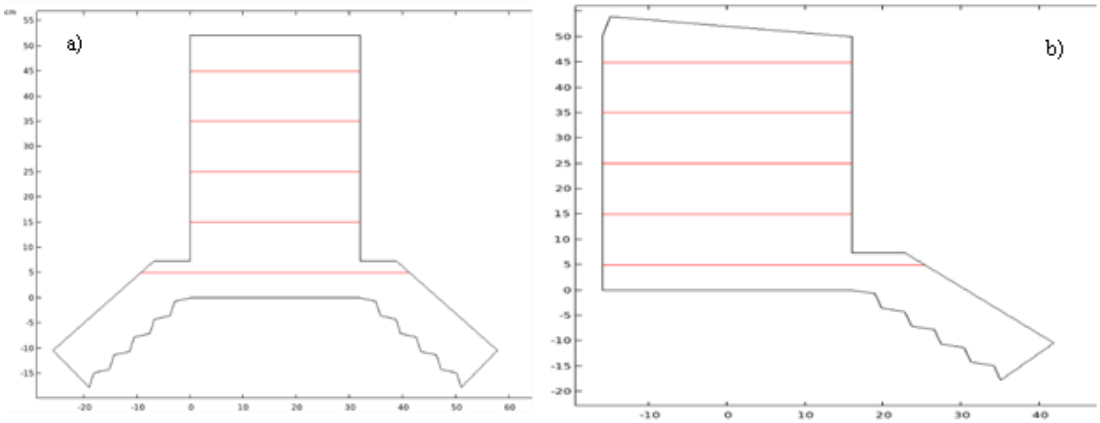

Fig. 8. Cross-sections of the solar device for obtaining results.
a) Symmetric construction, b) Asymmetric construction.

Figure 8 above shows numerical models representing the symmetric (a) and asymmetric (b) geometries used to optimize the thermal properties of the solar drying device. These models, with dimensions given in micrometers, are employed to analyze heat transfer and airflow distribution from the air collector to the drying chamber.

DISCUSSION

In this section, the characteristics of the flow dynamics and thermal distribution identified in the simulation results are discussed, specifically the analysis of the velocity, pressure, and temperature profiles at various vertical cross-sections (Distance = 0, 10, 20, 30, 40 cm). The velocity (V) profile in the following Figure 9 clearly shows how the airflow is distributed at different heights (z).

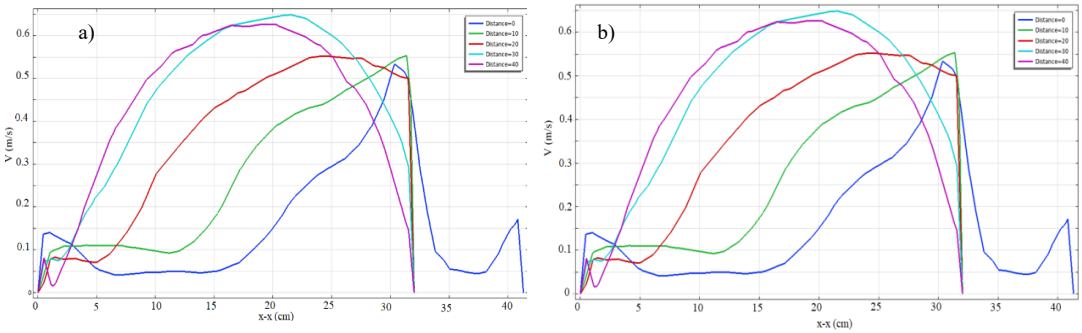

Fig. 9. Air velocity profiles at different heights within the drying chamber.
a) Air velocity distribution in symmetric geometry, b) Air velocity distribution in asymmetric geometry

The right graph (or graph (a) corresponds to the asymmetric geometry (part (b) of the previous Figure 7), revealing a pronounced asymmetry in the velocity distribution. The highest velocities are concentrated in a region shifted to one side (approximately x=25to 35 μm), rather than the center. This shift is a direct result of the asymmetric

design influencing the airflow path. Even at higher cross-sections, the maximum velocity remains displaced from the center, indicating non-uniform airflow within the drying chamber and varying convective efficiency across the width. Comparing these profiles is crucial for assessing how geometric changes impact air dynamics for optimal device performance.

The newly presented sequence of images reflects the results of the temperature (T) distribution for the symmetric and asymmetric geometries. These graphs show the variation of temperature (T) along horizontal cross-sections within the drying chamber of the solar drying device. Here, cross-sections along the vertical height (y) are isolated for thermal analysis.

Graph (a) in Figure 10 (corresponding to the symmetric geometry) shows a significant temperature rise (from 324 K to above 326 K) at the lowest height, closest to the chamber inlet. This increase occurs primarily in a small area from x=0 cm to 10 cm, indicating the entry of hot air from the collector and its immediate approach to the walls. However, in the central section (from x=10 cm to 40 cm), the temperature remains almost constant and very low, around 323.4 K, across all cross-sections. This suggests that the central zone lacks effective convective heat transfer or has low air velocity (as observed in the previous analysis). A slight secondary temperature increase is observed near the end of the chamber (from x=40 cm to 45 cm), which indicates the flow approaching the edges near the exit.

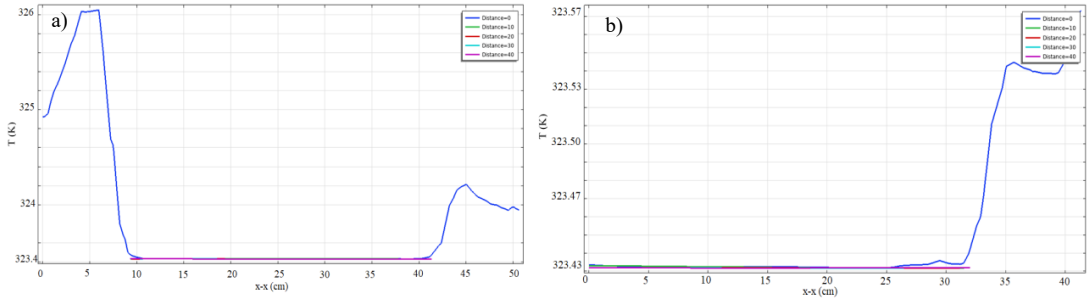

Fig. 10. Distribution of temperature (T) profiles across the geometries at different heights within the drying chamber; a) for symmetrical geometry, b) for asymmetric geometry

The second graph (corresponding to the asymmetric geometry) does not show the sharp temperature rise observed in the previous graph. Here, the temperature remains very low and constant (around 323.43 K) across almost all heights and a large part of the chamber (x=0 cm to 30 cm). Only near the end of the chamber (x=30 cm} 35 cm) does the blue line (Distance=0) rise significantly, reaching 323.54 K, which confirms the asymmetric concentration of the hot airflow towards one side. Overall, in both geometries, it was determined that the central part of the drying chamber-except for the lowest cross-section (Distance=0)-has a low temperature, which reduces its overall thermal efficiency. The asymmetric design, however, localizes the higher temperature to only a small section of the chamber.

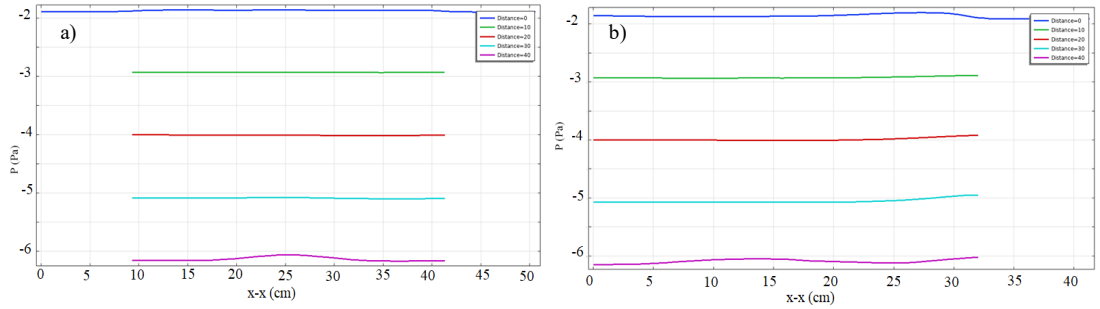

Fig. 11. Distribution of air pressure (P) profiles across the geometries at different heights within the drying chamber; a) for symmetrical geometry., b) for asymmetric geometry

Graphs (a) and (b) in Figure 11 show the air pressure distribution along horizontal cross-sections at various heights within the solar drying chamber. Graph (a), corresponding to the symmetric geometry, indicates that the

pressure in the central part is relatively more uneven (pink line) or stable (remaining cross-sections). Graph (b) represents the asymmetric geometry, where the pressure profile (particularly the pink line) is shifted towards one side, confirming a specific unidirectional flow tendency. These pressure variations directly affect the air flow dynamics inside the device, which in turn determine the efficiency and cost-effectiveness of the drying chamber. The small pressure differences are fundamental input data for analyzing natural convection movement.

In order to determine the reliability of the obtained results, heat dissipation from the absorber, as well as changes in velocity and pressure in the working chamber of the dryer, were calculated using the 'COMSOL MULTIPHYSICS 6.1' software, alongside results obtained from experimental tests. Figure 12 below presents the temperatures on the surface of the heating element from both experimental and numerical results when the solar radiation is in the range of 960–980 W/m^2.

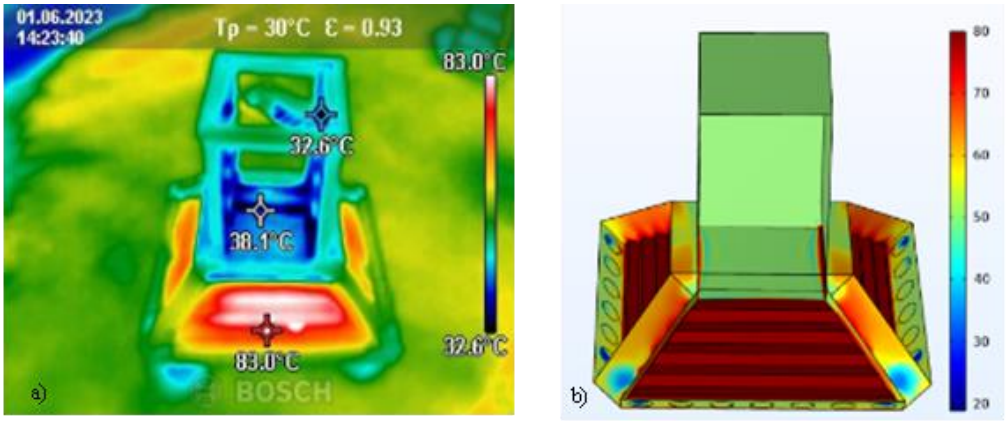

Fig. 12. Temperatures on the collector surface when the average solar radiation is 980 W/m^2
a) Thermographic (experimental) view, b) Numerical modeling resul.

Figure 12 presented above contains key results confirming the reliability of the study, where the temperature distribution on the absorber (collector surface) was compared using experimental (a) and numerical (b) methods under conditions where the solar radiation was in the range of 960–980 W/m^2. The experimental image (a), obtained via a thermal camera, records heating up to 83.0°C at the top part of the absorber, while the temperature in the central part is recorded at around 38.1ºC. This indicates that the heat is primarily concentrated near the walls of the absorber and at the top of the collector, while the temperature in the central flow remains relatively low.

The numerical modeling result (b) also reflects a similar picture of the temperature distribution: it indicates that the highest heating points are located at the edges and upper perimeter of the absorber. According to the color scale in the model result, these temperatures also represent values close to the experimental results. The fact that the numerical model results significantly replicate the location of the hottest and coldest spots in the experimental thermogram demonstrates the high degree of accuracy of the modeling of the device's internal processes. This, in turn, confirms the reliability of the computational method used in the COMSOL MULTIPHYSICS software for subsequent hydrodynamic and thermal analyses (the previously analyzed V and T profiles).

To confirm the reliability of the research, the relative error δ between the numerical modeling and experimental tests was calculated. For the temperatures on the absorber surface, under conditions where solar radiation was in the range of 960–980 W/m^2, the relative error was found to be between 2.5% and 3.8%. Such a low level of error indicates that the numerical model and its boundary conditions are capable of describing the internal hydrodynamic and thermal processes of the device with a high degree of accuracy. This serves as a basis for the reliability of the obtained velocity V and pressure P profiles.

CONCLUSION

The presented construction is newly developed, and a Utility Model patent (Patent No. FAP 2604) has been obtained for this specific design.

The relative error δ between the numerical model and experimental tests was determined to be between 2.5 % and 3.8 %, confirming the model's high accuracy. In the temperature analysis, the symmetric geometry showed a rapid drop in temperature, while the asymmetric design indicated that heat was localized to only a small section of the chamber.

The air velocity V profile in the symmetric device was high near the central axis, creating "dead zones" near the edges. In the asymmetric geometry, the flow profile was shifted to one side, and the pressure P profile was unevenly distributed, confirming a specific unidirectional airflow tendency.

Both geometries were found to have a low-temperature zone in the central part of the drying chamber, which reduces overall thermal efficiency. The results indicate the necessity of optimization by introducing flow-regulating elements to improve heat and mass transfer in the central zone.

ACKNOWLEDGMENTS

The author sincerely expresses gratitude to Fergana State Technical University for the financial support and laboratory facilities provided for the realization of this research.

REFERENCES

1. B. A. Basem *et al.*, “Investigating solar air collector performance with different absorber surfaces and Piranha fins through numerical simulation,” *Scientific Reports* **15**(1), 35361 (2025). https://doi.org/10.1038/s41598-025-19394-9
2. R. Venkatesh *et al.*, “Enhancement of solar dryer performance and collector efficiency of paraffin PCM/copper fin featured solar dryer,” *Scientific Reports* **15**(1), 31746 (2025). https://doi.org/10.1038/s41598-025-01555-5
3. S. Yematawu *et al.*, “Experimental testing on the performance of a solar dryer equipped with evacuated tube collector, rock bed heat storage and reflectors,” *Energy Reports* **12**, 453–471 (2024). https://doi.org/10.1016/j.egyr.2024.06.027
4. S. Radwan *et al.*, “Thermal performance analysis for three different geometric shapes of greenhouse-type solar dryer,” *Journal of Soil Sciences and Agricultural Engineering* **7**(11), 857–863 (2016). https://doi.org/10.21608/jssae.2016.40484
5. O. V. Ekechukwu and B. Norton, “Review of solar-energy drying systems II: An overview of solar drying technology,” *Energy Conversion and Management* **40**(6), 615–655 (1999). https://doi.org/10.1016/S0196-8904(98)00093-4
6. M. Daguenet, *Les séchoirs solaires: théorie et pratique* (UNESCO, Paris, 1985).
7. A. A. Gatea, “Design and construction of a solar drying system with a cylindrical section and performance analysis of the thermal drying system,” *African Journal of Agricultural Research* **6**, 343–349 (2011). https://doi.org/10.5897/AJAR10.347
8. L. Bennamoun, “An overview on application of exergy and energy for determination of solar drying efficiency,” *International Journal of Energy Engineering* **2**(5), 184–194 (2012). https://doi.org/10.5923/j.ijee.20120205.01
9. R. Bakari, “Heat transfer optimization in air flat plate solar collectors integrated with baffles,” *Journal of Power and Energy Engineering* **6**(1), 70–84 (2018). https://doi.org/10.4236/jpee.2018.61006
10. A. A. Yun, *Theory and Practice of Modeling Turbulent Flows with Heat Transfer, Mixing, Chemical Reactions, and Two-Phase Flows* (Moscow, 2009).
11. A. D. Girgidov, *Fluid and Gas Mechanics (Hydraulics)* (St. Petersburg, 2014).
12. J. Boussinesq, “Théorie de l’écoulement tourbillant,” *Mémoires de l’Académie des Sciences* **23**, 46–52 (1877).
13. P. R. Spalart, “RANS modelling into a second century,” *International Journal of Computational Fluid Dynamics* **23**(4), 291–293 (2009). https://doi.org/10.1080/10618560902940309
14. P. R. Spalart and M. Shur, “On the sensitization of turbulence models to rotation and curvature,” *Aerospace Science and Technology* **1**(5), 297–302 (1997). https://doi.org/10.1016/S1270-9638(97)90051-1